Published in final edited form as:
NMR Biomed. 2014 December ; 27(12): 1490–1501. doi:10.1002/nbm.3179.

Assessment of Lung Function in Asthma and COPD using Hyperpolarized 129Xe Chemical Shift Saturation Recovery Spectroscopy and Dissolved-Phase MR Imaging

Kun Qing, Ph.D.[1], **John P. Mugler III, Ph.D.**[1,2], **Talissa A. Altes, M.D.**[1], **Yun Jiang, M.S.**[3], **Jaime F. Mata, Ph.D.**[1], **G. Wilson Miller, Ph.D.**[1], **Iulian C. Ruset, Ph.D.**[4,5], **F. William Hersman, Ph.D.**[5,4], and **Kai Ruppert, Ph.D.**[1]

[1]Center for In-vivo Hyperpolarized Gas MR Imaging, Department of Radiology and Medical Imaging, University of Virginia, Charlottesville, VA, USA

[2]Department of Biomedical Engineering, University of Virginia, Charlottesville, VA, USA

[3]Department of Biomedical Engineering, Case Western Reserve University, Cleveland, OH, USA

[4]Xemed LLC, Durham, NH, USA

[5]Department of Physics, University of New Hampshire, Durham, NH, USA

Abstract

Magnetic-resonance spectroscopy and imaging using hyperpolarized xenon-129 show great potential for evaluation of the most important function of the human lung -- gas exchange. In particular, Chemical Shift Saturation Recovery (CSSR) xenon-129 spectroscopy provides important physiological information for the lung as a whole by characterizing the dynamic process of gas exchange, while dissolved-phase xenon-129 imaging captures the time-averaged regional distribution of gas uptake by lung tissue and blood. Herein, we present recent advances in assessing lung function using CSSR spectroscopy and dissolved-phase imaging in a total of 45 subjects (23 healthy, 13 chronic obstructive pulmonary disease (COPD) and 9 asthma). From CSSR acquisitions, the COPD subjects showed red blood cell to tissue/plasma (RBC-to-TP) ratios below the average for the healthy subjects ($p<0.001$), but significantly higher septal wall thicknesses, as compared with the healthy subjects ($p<0.005$); the RBC-to-TP ratios for the asthmatics fell outside 2 standard deviations (either higher or lower) from the mean of the healthy subjects although there was no statistically significant difference for the average ratio of the study group as a whole. Similarly, from the 3D DP imaging acquisitions, we found all the ratios (TP-to-GP, RBC-to-GP, RBC-to-TP) measured in the COPD subjects were lower than those from the healthy subjects ($p<0.05$ for all ratios), while these ratios in the asthmatics differed considerably between subjects. Despite having been performed at different lung inflation levels, the RBC-to-TP ratios measured by CSSR and 3D DP imaging were fairly consistent with each other, with a mean difference of 0.037 (ratios from 3D DP imaging larger). In ten subjects the RBC-to-GP ratios obtained from the 3D DP imaging acquisitions were also highly correlated with their DLCO/Va ratios measured by pulmonary function testing ($R=0.91$).

Corresponding Author (current address): Kai Ruppert, Children's Hospital of Cincinnati, 3333 Burnet Ave., MCL 5033, Cincinnati, OH 45229, Phone: (513) 803-4826, Fax: (513) 636-3754, kai.ruppert@cchmc.org.

Keywords

Hyperpolarized xenon-129; CSSR; 3D dissolved-phase imaging; gas uptake; COPD; asthma; pulmonary imaging

INTRODUCTION

Magnetic resonance imaging using hyperpolarized noble gases provides powerful tools for evaluating pulmonary structure and function by obtaining information from the lung airspaces. In the past, most imaging research in humans has been performed using hyperpolarized helium-3 (HHe) (1-3). However, hyperpolarized xenon-129 (HXe) has recently begun to draw increasing attention (4). In part, this is due to the skyrocketing market price for helium-3 caused by an expansion in demand for use in neutron detectors in conjunction with the non-renewable nature of the helium-3 supply, which has greatly increased the cost for HHe MRI studies. In addition, improvements in xenon polarizer design (5) have led to devices that can produce liter quantities of HXe at polarizations up to 50%. As a result, HXe ventilation images now rival the quality of HHe images. Furthermore, xenon has a much higher Ostwald solubility than helium in many tissues, including blood (6), and exhibits a large nuclear magnetic resonance chemical shift, on the order of 200 ppm, due to environmental change (7), making it easily discernible from xenon in the free gas phase. Following inhalation, most HXe stays in the lung airspaces, where it gives rise to a dominant “gas-phase” (GP) peak in a spectrum (by definition at 0 ppm). In contrast, only about 1-2% of HXe in the lung dissolves into the parenchyma and blood, yielding so-called “dissolved-phase” (DP) xenon and resulting in two additional, smaller spectral peaks. These peaks have been assigned to HXe dissolved in either the lung tissue or blood plasma (the “tissue-plasma” or TP peak at about 198 ppm), and to HXe dissolved in the red blood cells (the RBC peak at about 218 ppm) (8-11). The quantitative characteristics of DP xenon are determined by the surface-to-volume ratio (12) and important physiological factors, such as, gas-blood barrier wall thickness (13), alveolar tissue density (14), and pulmonary perfusion (15,16), which, if known, could be very useful for assessing pulmonary gas exchange, as well as for detection and treatment of many lung diseases.

Once inhaled, xenon quickly diffuses into the lung parenchyma and blood, and is carried away by the cardiovascular circulation. Gas exchange between the alveolar airspaces and the lung parenchyma is sufficiently rapid to establish a dynamic equilibrium between the DP pool and the GP pool at the gas-exchange site within a few tens of milliseconds. The dynamic nature of pulmonary xenon gas exchange can be investigated by xenon uptake spectroscopy, commonly referred to as “chemical shift saturation recovery” (CSSR) MR spectroscopy (10,15,17,18). Fitting of the CSSR measurement data to gas exchange models (19-22) allows extraction of physiologically relevant functional parameters that characterize the xenon gas-exchange properties of the lung, and has already proven to be valuable for identification of global pathological changes in the lungs of subjects with interstitial lung disease or COPD (20).

Recently, it has also become feasible to move beyond spectroscopic measurements and image DP xenon in the lung directly (23-27). Aiming at future clinical applications, it is highly desirable to acquire DP and GP images in a single breath hold, because the absolute DP signal itself has limited physiological relevance as it would not be possible to differentiate whether regional variations are caused by heterogeneity in gas uptake versus heterogeneity in ventilation. Using the findings of Ruppert et al. (28) and Driehuys et al. (13) in animal studies, Qing et al. (29) developed a method permitting regional mapping of both ventilation and of the fractions of HXe dissolved in the TP and RBC compartments from multi-echo three-dimensional (3D) data acquired during a single breath hold, with a duration easily tolerated by most subjects. The multi-echo 3D radial sequence was designed to collect three echoes from the DP magnetization and two echoes from the GP magnetization during the same acquisition. The Hierarchical IDEAL method (30), a multi-point Dixon-based method that was originally designed for fat-water separation, was employed to separate the two dissolved-phase components using the three DP echoes, while taking advantage of the field map obtained from the two GP echoes, which are also reconstructed as ventilation images, as an initial estimate of the B_0 field.

In this work, we present recent advances in the assessment of subjects with COPD or asthma using CSSR spectroscopy and 3D DP imaging, and compare these findings with those from healthy subjects. Further, we explore the correlation between the two techniques, and discuss their future development.

MATERIALS AND METHODS

Human Subjects

A total of 45 subjects (23 healthy, 13 COPD and 9 asthma) underwent HXe MRI for this preliminary investigation. The septal wall thicknesses for 5 of the healthy subjects (H5, H20-H23) obtained from lung-inflation dependent CSSR measurements were acquired with a different RF coil (the rigid, linearly-polarized RF coil, see below) than that used for the other subjects. Hence, these 5 subjects were not included in the subsequent comparisons of the CSSR-based DP xenon ratios between healthy subjects and subjects with lung disease. Of the remaining 40 subjects, we show the 3D DP imaging results for 21 subjects (11 healthy: H1-H11, 6 COPD: C1-C6, and 4 asthma: A1-A4), and CSSR spectroscopy results for 30 subjects (11 healthy: H9-H19, 10 COPD: C3-C11, C13 and 9 asthma: A1-A9). Among them, 11 subjects (3 healthy: H9-H11, 4 COPD: C3-C6, and 4 asthma: A1-A4) underwent both 3D DP imaging and CSSR spectroscopy. Subject H12 was clinically healthy but had a history of high exposure to second-hand smoke. (Data from 5 of the healthy subjects: H1, H4-H7, 3 of the COPD subjects: C2, C4, C6, and 2 of the asthmatics:A2, A4, were previously reported in (29) for 3D DP imaging.) For 11 of the subjects (4 healthy: H1-H3, H7, 4 COPD: C1, C2, C4, C6, and 3 asthma: A1, A3, A4) who underwent 3D DP imaging, the diffusing capacity of the lung for carbon monoxide (DLCO) was also measured. The demographic information and relevant pulmonary function test results are shown in Table 1.

MR Study Procedures

Immediately before and after each MR study, spirometry was performed using a hand-held device (Koko; PDS Ferraris, Louisville, CO), and 12-lead electrocardiography (HP Pagewriter XLi; Hewlett Packard Co., Palo Alto, CA) was performed for subjects 40 years and older. (Forced expiratory volume in one second [FEV_1] values provided in the text are percent-predicted.)

Female subjects underwent a urine pregnancy test before imaging and were excluded from participation if found to be pregnant. A test dose of xenon gas (not hyperpolarized) was administered before the MR study, and the subject was excluded from participation if the subject felt that the side effects from the test dose were too unpleasant. Hyperpolarized xenon MRI has an excellent safety record (31,32) and only a very small fraction of subjects recruited at our site has ever reported intolerable side effects that precluded them from study participation. Throughout the imaging session the subject's heart rate and oxygen saturation levels were monitored (3150 MRI Patient Monitor; Invivo Research Inc., Orlando, FL), and central nervous system side effects of the inhaled xenon on the subjects were assessed. All studies were supervised by a physician.

Enriched xenon gas (87% xenon-129) was polarized by collisional spin exchange with an optically-pumped rubidium vapor in a prototype commercial system using the flow approach (XeBox-E10; Xemed, LLC, Durham, NH), providing gas polarizations of approximately 40% (5,33). MR acquisitions were performed using a 1.5T commercial whole-body MR scanner (Avanto; Siemens Medical Solutions, Malvern PA). A flexible, circularly-polarized, vest-shaped chest RF coil (Clinical MR Solutions, Brookfield, WI) or a rigid, custom-built, linearly-polarized chest RF coil was used for the HXe acquisitions. Both coils were blocked at the proton resonance frequency to allow proton MRI with the scanner's body coil to be performed with the xenon RF coil in place.

CSSR Spectroscopy Acquisition

CSSR Study Protocol—In 5 of the healthy subjects, the dependence of the DP xenon ratios and the septal wall thickness on lung inflation was assessed. Data was collected at three different lung inflation levels:

1. Residual Volume (RV): Starting from RV, the subjects inhaled 0.8 L of HXe, continued with inhalation of room air until they reached their total lung capacity (TLC), then exhaled to RV and held their breath. Note that the measurements were performed at the true RV and therefore are likely to differ somewhat from similar breathing maneuvers reported in the literature that entailed the inhalation of a small volume of HXe starting from RV.
2. 50% of Forced Vital Capacity (FVC): Starting from RV, the subjects inhaled 0.5 L of HXe, continued with inhalation of room air from a second dose bag containing a predetermined volume to reach a total lung inflation of 50% FVC, and then held their breath.

3. Total lung capacity: Starting from RV, the subjects inhaled 0.5 L of HXe, continued with inhalation of room air until they reached their TLC, and then held their breath.

All other CSSR studies were performed with the subjects holding their breath at TLC as described for the third breathing maneuver above.

Pulse Sequence Protocol and Data Analysis—The CSSR spectroscopy pulse sequence consisted of four repeating elements (Fig. 1a): 1) Selective RF saturation of the DP resonances followed by gradient spoiling of residual transverse magnetization; 2) a delay time τ between RF saturation and RF excitation; 3) RF excitation of the GP and DP resonances; and 4) sampling of the free induction decay (FID). Due to the size of a human chest RF coil and the power limitations of broadband amplifiers in clinical MR systems, it is frequently not possible to employ individual 90° RF saturation pulses that have a sufficiently large bandwidth to completely saturate all DP resonances at the same time. For instance, at 1.5T, a Gaussian RF pulse would have to be shorter than 1 ms to saturate the entire DP region in a human lung spectrum. Therefore, we implemented a 3-pulse RF saturation scheme that consisted of lower bandwidth, 2-ms 90° Gaussian pulses applied first at 198 ppm (TP), then at 218 ppm (RBC) and finally at 208 ppm (between TP and RBC resonances), followed by a short spoiler gradient. These pulses were spaced 3 ms apart. To minimize unintended spin-inversion effects in the overlapping frequency bands, each RF pulse also had a different phase (180°, 0°, 90°). A 1.2-ms Gaussian RF excitation pulse was used to generate a free induction decay, which was sampled for 30.72 ms with 1024 sampling points. A total of 32 spectra were acquired during each breath hold.

The delay time τ between the final saturation RF pulse and the excitation RF pulse determines the time period during which highly-polarized xenon atoms from the alveolar airspaces can enter lung tissue and replenish the depleted DP magnetization. Two different protocols were used for the CSSR acquisition. To sample the xenon gas-uptake curve, which is required to extract information about the septal wall thickness, τ was varied from 3 ms to 900 ms for the 32 spectral acquisitions within a breath hold. To improve the signal-to-noise ratio (SNR) for the quantification of the spectral-peak ratios, and to temporally average out the impact of pulsatile blood flow, τ was held fixed at 100 ms for all 32 acquisitions in a breath hold. The repetition time for any given spectral acquisition was equal to τ + 40 ms.

Post-processing and data analysis were performed using MATLAB (MathWorks, Natick, MA, USA). The sampled data were apodized by a squared cosine function, zero-filled to 2048 points, Fourier transformed and phased to first order. The GP peak area was determined analytically by fitting a Gaussian function to the GP resonance. Especially for short delay times, the real part of the two dissolved-phase resonances, RBC and TP, deviated too much from an ideal Gaussian or Lorentzian line shape for analytical fitting and, thus, were integrated numerically. For the studies with fixed τ, the ratios of TP-to-GP, RBC-to-GP, and RBC-to-TP were calculated individually for each spectrum from a breath hold and then averaged. Averaging over 32 separate measurements within the same breath hold not only increased the signal-to-noise ratio but also minimized the impact of pulsatile variations in the HXe uptake rate (due to the cardiac cycle), particularly for the RBC peak (34). To

assess the septal wall thickness from the xenon uptake curve, the area under the TP peak as a function of τ was fitted to the model described by Patz et al. in (20), as illustrated in Fig. 1b. Assuming a HXe diffusion constant in tissue of 3.3×10-6 cm^2/s (19) permitted calculation of the septal wall thickness. Statistical significance for differences in the spectroscopic findings was assumed for p-values of less than 0.05 in two-tailed t-tests with unequal variances and was calculated using Excel 2010 (Microsoft, Redmond, WA, USA).

3D Dissolved-phase Imaging

Pulse Sequence Protocol—Three-dimensional DP imaging was performed using the method introduced above from Qing et al (29); the method and associated data analysis are described briefly here. A multi-echo 3D radial pulse sequence was used to acquire three echoes for the DP ($TE_1/TE_2/TE_3$=0.74/2.36/3.98 ms) and two echoes for the GP (TE_1/TE_2=0.74/2.36 ms) during interleaved repetitions. An image was calculated for each echo. An optimized low-flip-angle excitation RF pulse with negligible sidebands (reject-band ripple, 0.001%; duration, 1.3 ms), designed using the Shinnar-Le Roux algorithm incorporated into the open-source MATPULSE tool (version 5.1) (35), was used to independently excite the DP and GP magnetization during interleaved repetitions. To achieve the maximum SNR for a TR of 19 ms, a flip angle of 23° was used for the DP excitations and a flip angle of 0.4° for the GP excitations. The resulting total acquisition time was 11 sec. Three-dimensional image sets of the whole lung were acquired with a voxel volume of 7.6 × 7.6 × 17 mm^3 (the largest voxel dimension was in the anterior-posterior direction). Due to the short T2* of the DP signal of about 2 ms (36), it is beneficial to collect data with the shortest TE possible. Therefore, a half-echo radial (radial-out) acquisition was used for the first echo of both DP and GP image acquisitions, undersampled to yield an acceleration factor of 2.8, while full echo radial (radial-in-and-out) acquisitions corresponding to acceleration factor of 1.4 were collected for the other echoes (29). The 3D radial spokes were arranged according to the golden-angle method (37). All DP RF excitation pulses were applied midway between the two DP resonances (3,660 Hz from the GP resonance at 1.5T). All subjects inhaled 1 L of HXe mixed with N_2 to one-third of FVC, starting from RV, and then held their breath for the acquisition.

Image Reconstruction and Post-processing—The quadratic penalized weighted-least-squares (QPWLS) via preconditioned conjugate gradients (PCG) algorithm (38) was used to reconstruct the undersampled 3D-radial image sets. The two DP signal components were separated using the Hierarchical IDEAL method (30). To improve separation efficiency and accuracy, reference B_0 maps calculated from the two GP images were employed as an initial field map estimate. For the quantitative comparison among subjects, four signal ratios were calculated based on the acquired GP and DP signals, as described in (29): total DP-to-GP, TP-to-GP, RBC-to-GP, and RBC-to-TP. For the first three ratios, a mask created from the xenon ventilation images using a signal-intensity-based threshold was applied to regionally restrict the ratio maps to ventilated lung areas. The RBC-to-TP ratio was subsequently employed as a secondary mask to exclude regions with high RBC but low TP signal, such as the heart. The three types of coronal ratio maps shown in this work, TP-to-GP, RBC-to-GP, and RBC-to-TP, are scaled from 0.0 to 1.5%, 0.0 to 0.8%, and 0.0 to 0.7, respectively.

Correlation with DLCO—As one of the most clinically valuable tests of lung function, DLCO measures the ability of the lungs to transfer gas from inhaled air to the RBCs in pulmonary capillaries. For ten subjects (4 healthy: H1-H3 and H7, 3 COPD: C1, C2 and C4, and 3 asthma: A1, A3 and A4; Table 1) with both 3D DP imaging and DLCO results, we calculated the correlation coefficient between the whole lung RBC-to-GP ratios obtained from 3D DP imaging and the DLCO per unit alveolar volume ratio (DLCO/Va), since both techniques provide information about the amount of gas transferred to the blood vessels in the gas exchange area relative to the size of the ventilated volume. (Note that because COPD subject C6 had difficulty inhaling the total volume of gas, which resulted in a relatively low SNR for the DP images, the TP and RBC components could not be separated and thus this subject is not included even though DLCO was performed.)

Correlation and Comparison between the 3D DP Image and CSSR Acquisitions

Correlation Investigated by Numerical Simulation—CSSR spectroscopy measurements suggest that xenon uptake by the lung parenchyma can be envisioned as the combination of two processes (19,20). The first process is the rapid saturation of the stationary lung tissue, which occurs on the time scale of approximately 100 ms and is nonlinear in time. The second process, approximately linear in time, is the downstream accumulation of HXe in the flowing blood and in tissue outside the immediate gas-exchange region to which magnetization has been transported by the circulation. During the 3D DP acquisition with a flip angle of 23° and a TR of 19 ms, a static DP signal pool would be consumed by only a few RF excitations. However, fresh xenon magnetization is continuously entering the TP compartments from the alveolar airspaces, replenishing the DP magnetization available for imaging. Hence, it can be expected, as long as any T1 effects are neglected, that shortly after the image acquisition has begun the DP magnetization distribution will approach a steady state. We took advantage of the xenon gas-exchange model proposed in (20) to investigate the signal evolution during the 3D DP acquisition in an attempt to understand how the image-based results compare to those from CSSR spectroscopy acquisitions.

For simplification, as in (20), the DP magnetization is treated as a single, homogeneous pool with a flow component linear in time. Using gas-exchange and blood-flow parameters averaged from representative xenon-uptake curves (Fig. 1b) acquired in three healthy volunteers, the xenon gas-exchange model was used to generate the DP longitudinal magnetization versus delay time for a CSSR acquisition; below, this is referred to as the simulated CSSR xenon-uptake curve. Numerical simulations for 3D DP imaging were then conducted, using MATLAB, based on the following five steps: 1) The starting DP longitudinal magnetization is set to the value corresponding to a delay of 2 s on the simulated CSSR xenon-uptake curve, since this time delay is representative of that between the end of inspiration and the start of imaging; 2) The DP longitudinal magnetization immediately following an excitation RF pulse is calculated as the DP longitudinal magnetization just before the pulse times the cosine of the flip angle for the excitation RF pulse; 3) The delay time on the simulated CSSR xenon-uptake curve that corresponds to the DP longitudinal magnetization just after the RF pulse is determined; 4) The DP longitudinal magnetization immediately before the next excitation RF pulse is determined from the

simulated CSSR xenon-uptake as the value at a delay time equal to TR plus the delay determined in step 3 (this accounts for the ongoing gas exchange between the GP and DP pools); and 5) Steps 2 through 4 are repeated for all RF pulses in the 3D DP image acquisition. The steady-state value (assuming the gas-phase signal is constant and neglecting T1 relaxation) of the delay time is designated the equivalent delay time.

Direct Comparison of the Measured RBC-to-TP Ratios—The results from 3D DP imaging and CSSR spectroscopy measurements are not directly comparable, because, on one hand, they were collected at different lung inflation levels (3D DP imaging at one-third FVC, CSSR at TLC), and, on the other hand, the detected signals originate from different underlying DP magnetization distributions, as will be described further in the discussion section. Thus, we only compared the whole lung RBC-to-TP ratios measured by both techniques in this work, because they seemed to have the least dependency on lung inflation levels compared to the other ratios. Because of the low SNR obtained for the DP in COPD subject C6, 10 subjects (3 healthy: H9-H11, 3 COPD: C1-C3, and 4 asthma: A1-A4) were included in this direct comparison.

RESULTS

CSSR Spectroscopy Acquisition

For the subgroup of 5 healthy subjects included in this part of the study, the averaged xenon signals from the TP and RBC dissolved-phase compartments in the lung, relative to that from the alveolar GP, and relative to each other, were strongly dependent on lung inflation level as illustrated in Fig. 2a-c (39). At RV, the TP-to-GP ratio was about two times higher, the RBC-to-GP ratio was about 3.5 times higher, and the RBC-to-TP ratio was about 1.5 times higher than the respective values at TLC. At each inflation level, each of the TP-to-GP and RBC-to-GP ratios was significantly different from the others ($p < 0.01$). The RBC-to-TP ratio was only significantly different between RV and TLC ($p < 0.01$). The average septal wall thickness, on the other hand, remained largely unchanged as lung inflation was increased from RV to 50% FVC, and was found to be only about 7% and 10% lower at TLC than at RV and 50% FVC, respectively (Fig. 2d); neither difference was statistically significant ($p = 0.2$ and $p = 0.08$, respectively). Since these measurements were performed in the rigid, linearly-polarized RF coil, which had different RF characteristics than the circularly-polarized vest coil employed for all the other CSSR studies, these xenon ratios were not included in the comparisons between healthy and diseased subjects to prevent the introduction of this confounding factor. Nevertheless, the observed relative changes caused by differences in lung inflation are valid in all cases.

The average septal wall thickness as measured by CSSR spectroscopy at TLC showed a strong dependence on the subjects' health status. For example, Figure 3 shows the measurements of septal wall thickness at TLC in 24 subjects, color-coded by status (healthy, second-hand smoker (SHS) or COPD), and sorted by increasing thickness (from left to right). This simple approach separated, to a large degree, the healthy subjects (median wall thickness: 7.1± 0.9 μm) from the clinically healthy second-hand smoker (wall thickness: 11.4 μm) and the COPD subjects (median wall thickness: 11.9 ± 3.7 μm) (39). The

difference between the healthy and COPD groups was statistically significant ($p < 0.005$). Further, the alveolar walls in GS 0 and GS 1 subjects appeared to be thicker than in healthy subjects, but thinner than in the GS 2 and GS 3 subjects. Nevertheless, the number of subjects in these subgroups was too small for a meaningful statistical analysis of this possible correlation.

Similarly, the average RBC-to-TP ratios measured at TLC also demonstrated a strong dependence on the subjects' health status. The RBC-to-TP ratios for 29 subjects are plotted in Fig. 4. The ratios for 12 of the 13 healthy subjects were confined to a narrow range from about 0.24 to 0.32, with an average value of 0.29 ± 0.039 . For almost all 20 subjects with lung disease, the RBC-to-TP ratios fell outside of 2 standard deviations from the mean of the healthy subjects. Interestingly, the RBC-to-TP ratios for asthmatic subjects seemed to be either above or below the range for the healthy subjects, but the average value showed no statistically significant difference (0.31 ± 0.12 , $p = 0.76$). On the other hand, the RBC-to-TP ratios for all COPD patients were below the average for the healthy subjects (average value: 0.15 ± 0.05 , $p < 0.00001$). No correlation between RBC-to-TP ratio and GOLD stage was apparent for the COPD subjects (not shown) but, again, too few subjects have been studied to draw conclusions. In this work the RBC-to-TP ratios were analyzed for a delay time of 100 ms. However, since in most subjects the septal wall thickness was assessed by a CSSR sequence with variable delay time, the RBC-to-TP ratio can be quantified for the entire range of delays. Nevertheless, beyond the first tens of milliseconds, we found the RBC-to-TP ratio to be largely independent of the delay time. For delay times shorter than that the RBC peak, in particular, was much noisier than the TP peak, which would explain the instability of the RBC/TP ratio in this regime. This behavior was similar for all subjects.

3D Dissolved-phase Imaging

Healthy Subjects—Signal ratios obtained from the young healthy subjects (N=8, H4-H11, age 18-32 yrs), averaged over the lung, showed relatively minor variation among subjects as illustrated in Fig. 5. The TP and RBC images, and the corresponding ratio maps (TP-to-GP, RBC-to-GP and RBC-to-TP), were generally homogeneous within coronal slices. No ventilation defects were observed. Figure 6 shows representative images and ratio maps acquired in healthy subject H6 (adapted from (29) with permission). The older healthy subjects (N=3, H1-H3, age > 50 yrs) had lower whole-lung RBC-to-TP ratios (Fig. 5) as compared to the younger subjects and exhibited some minor ventilation defects. The means and standard deviations of the ratios for all healthy subjects were $1.38\% \pm 0.15\%$ for the DP-to-GP ratios, $1.19\% \pm 0.14\%$ for the TP-to-GP ratios, $0.34\% \pm 0.06\%$ for the RBC-to-GP ratios and 0.28 ± 0.05 for the RBC-to-TP ratios.

COPD Subjects—In general, HXe gas uptake by the lung in subjects with COPD (C1-C6) was decreased compared to that in healthy subjects. The whole-lung DP-to-GP, TP-to-GP and RBC-to-GP ratios (mean ± standard deviation, Fig. 5) for the 6 COPD subjects were $0.89\% \pm 0.26\%$ ($p < 0.001$), $0.88\% \pm 0.17\%$ ($p < 0.005$), and $0.19\% \pm 0.08\%$ ($p < 0.001$), respectively. One subject at GS 1 (COPD subject C2 in Fig. 5, FEV_1/FVC 0.69, FEV_1 83%) had a whole-lung RBC-to-TP ratio close to or slightly higher than that for healthy subjects. Nonetheless, the mean RBC-to-TP ratio for all of the COPD subjects was 0.20 ± 0.08,

significantly less than that for healthy subjects ($p < 0.05$). This relationship for the whole-lung RBC-to-TP ratios in COPD subjects compared to those in healthy subjects is consistent with the finding from CSSR spectroscopy, and, despite the methodological differences, quantitative values derived from the two techniques were generally similar.

Figure 5 illustrates that all ratios in subjects at GS 2 or 3 were lower than those in healthy subjects and lower than those in COPD subjects at GS 1. Figure 6 shows representative HXe ventilation, TP and RBC images, as well as the TP-to-GP, RBC-to-GP and RBC-to-TP ratio maps, acquired from COPD subject C3 (GS 2, FEV_1/FVC 0.54, FEV_1 64%) and subject C4 (GS 3, FEV_1/FVC=0.57, FEV_1 39%). The lungs of both subjects exhibited numerous ventilation defects. The whole-lung TP-to-GP ratios (0.77% and 0.85%) and RBC-to-TP ratios (0.12 and 0.16) in these two subjects were much lower than those in healthy subjects (mean 1.19%, and 0.28, respectively), and the overall gas uptake by the RBCs (0.09% and 0.13%) was only about one-third of the mean value in the healthy subjects (0.34%). Interestingly, COPD subject 3 at GS 2 actually had lower DP ratios than COPD subject 4, who was at GS 3 and thus had decreased spirometric indices. This might suggest that the functioning parts of the lung in COPD subject 3 were performing worse than those in COPD subject 4.

Asthma Subjects—Among the three young asthmatics (A1-A3, age 16-26 yrs), two of them (subject A2, age 16 yrs, FEV_1/FVC 0.73, FEV_1 100%; subject A3, age 26 yrs, FEV_1/FVC 0.60, FEV_1 80%) showed higher whole-lung RBC-to-TP ratios (0.43 and 0.51) than all of the healthy subjects (mean 0.28, Fig. 5d), but their whole-lung TP-to-GP ratios (0.60% and 0.66%) were very low, even lower than those of COPD subjects (mean 0.88%, Fig. 5b). Representative HXe ventilation, TP and RBC images, and the corresponding TP-to-GP, RBC-to-GP and RBC-to-TP ratio maps, for asthma subject A2 are shown in Fig. 6. Despite ratio values that differ from those of healthy subjects, the TP-to-GP and RBC-to-TP ratio maps were relatively homogeneous. All whole-lung ratios in the older asthmatic (subject A4, age 53 yrs, FEV_1/FVC 0.56, FEV_1 95%) were low compared to those in healthy subjects, and similar to those in COPD subjects. The ratio maps were also inhomogeneous. For example, in the coronal slice shown in Fig. 6, the TP-to-GP ratios were elevated, but RBC-to-GP and RBC-to-TP ratios were decreased, in the right upper lobe of the lung compared to other regions in the same slices. One young asthmatic (subject A1, age 26 yrs, FEV_1/FVC 0.60, FEV_1 80%) appeared to be different than the other asthmatics, as this subject did not show obvious ventilation defects. Also, the whole-lung DP-to-GP and TP-to-GP ratios were slightly higher than those in healthy subjects, while the whole-lung RBC-to-TP ratio was at the low end of the values in healthy subjects.

Analogous to the behavior seen for COPD, the relationship for the whole-lung RBC-to-TP ratios in asthma subjects compared to those in healthy subjects is consistent with the finding from CSSR spectroscopy, wherein the values in asthmatics tended to be either above or below those for healthy subjects, and the quantitative values derived from the two techniques were generally similar.

Correlation with DLCO/Va—The RBC-to-GP ratios obtained from ten subjects are plotted against the corresponding DLCO/Va ratios in Fig. 7. A relatively high correlation coefficient (R=0.91) was found for the two data sets.

Correlation and Comparison between the 3D DP Image and CSSR Acquisitions

Results from the numerical simulations are summarized in Fig. 8. For two septal wall thicknesses, the figure shows examples of the calculated recovery of the DP longitudinal magnetization following a saturation RF pulse due to gas uptake into lung tissue (simulated CSSR xenon-uptake curves, left column) and the associated evolutions of the DP longitudinal magnetization during the 3D acquisition (middle column). The plot in the right column shows the delay time for the CSSR acquisition that corresponds to the steady state for the 3D acquisition (denoted the equivalent delay time) as a function of the septal wall thickness. These results indicate that the DP magnetization quickly reaches steady state during the 3D acquisition (neglecting relaxation). For instance, for a septal wall thickness of 6 μm (at the lower end of values for healthy subjects, see Fig. 3), the signal reaches steady state after about 17 RF excitations (Fig. 8c). In the 3D DP acquisition 520 RF excitations are applied, although the signals corresponding to the first 20 are discarded to avoid the initial transient behavior of the signal evolution (29).

The model (20) on which the simulations are based can be used to extract three important physiological parameters: the lung surface-to-volume ratio, the alveolar septal wall thickness and the mean capillary transit time. Most subjects' mean capillary transit time quantified as a byproduct of our CSSR measurements was found to be approximately 1 second (results not shown). By using this value in our simulations, the equivalent delay time for the 3D DP acquisition was found to be independent of the surface-to-volume ratio, but dependent on the alveolar septal wall thickness. For example, at a wall thickness of 6 μm, the equivalent delay time was about 26 ms, as indicated in Fig. 8a. However, for a wall thickness of 20 μm (approximately the highest value found in COPD subjects), this corresponding delay time increases to 100 ms, albeit at a 30% lower steady-state longitudinal magnetization. The plot in Fig. 8e indicates that, as the septal wall gets thicker, the 3D DP imaging pulse sequence corresponds to a longer delay time for the CSSR spectroscopy acquisition. Thus, the 3D DP imaging results presented herein are predicted to correspond to equivalent delay times that are similar to, but generally a bit less than, the value of 100 ms used for the CSSR data presented in Fig, 4. The correspondence observed between experimental values from CSSR and 3D DP imaging is consistent with this theoretical prediction, wherein the CSSR and imaging results show the same trends, and quantitatively similar, but not identical, values.

A Bland-Altman plot of the RBC-to-TP ratios measured by 3D DP imaging and those measured by CSSR is shown in Fig. 9. All points fall within the 95% confidence intervals. The mean difference between the two data sets (3D DP Imaging - CSSR) is 0.037 ± 0.036. Considering that the CSSR measurements were performed at higher lung inflation level than the 3D DP imaging studies, lower RBC-to-TP ratios for CSSR were to be expected.

DISCUSSION

The inflation level of the lung at which subjects hold their breath during data acquisition has tremendous impact on the quantification of xenon DP parameters. From maximum lung inflation at TLC to maximum deflation at RV, whole-lung RBC-to-GP ratios in healthy subjects increased, on average, by more than 250%. Although the decrease in tissue density per unit volume with increasing inflation is a driving factor for this effect, it is interesting to note that, over the same range, TP-to-GP ratios increased only by approximately 120%. At a delay time τ of 100 ms as used for the associated CSSR spectroscopy measurements, lung tissue in the immediate vicinity of the gas exchange sites is generally saturated with xenon magnetization. Considering that the total volume of static lung tissue does not change during respiration, a plausible explanation for this observation would be that the blood volume in the pulmonary microvasculature involved in HXe gas exchange was roughly 40% lower at TLC than at RV due to the stretch-induced increase in capillary flow resistance.

On one hand, a large dynamic range in a measured parameter is very desirable because, for a given SNR, it facilitates detection of relatively small variations that could be associated with pathological changes in lung physiology. On the other hand, a large parameter variability within the normal respiratory cycle can easily mask abnormal changes when the ventilation level at which data is collected cannot be carefully controlled. To the best of our knowledge, this problem is usually addressed in hyperpolarized noble-gas MRI studies by attempting to acquire data at a predefined lung inflation level. This level can be a physiological extreme such as RV or TLC, or a level that is achieved following inhalation of a certain gas volume from RV, which is either a fixed volume or based on physiological volumes such as a selected fraction of the lung capacity. The main weakness of this approach is that the reproducibility is, to a large extent, dependent on subject effort, motivation and, particularly in the case of patients with more severe lung disease, physical ability. The subsequent MR measurement during a breath hold is assumed to have taken place at the targeted lung inflation level regardless of the inflation level that was actually achieved. A different way of addressing the problem would be to obtain an independent assessment of the lung inflation level at which the measurement took place, and then to correct the value of the parameters obtained with respect to a normalized lung inflation level. For our future work, we thus envision the HXe acquisition to be bracketed by rapid 2D proton acquisitions, all obtained within the same breath hold. These two proton acquisitions can then be compared to determine whether the breath hold was performed at a constant diaphragm position. Also, the images can be retrospectively referenced to additional, independent proton MR scans collected at RV and TLC. If a breath-hold HXe acquisition at a targeted inflation level is combined with such proton reference scans, we believe it will be feasible to largely remove the physiologic variability of the lung inflation level by a first-order parameter correction, and thereby take full advantage of the large dynamic range in the DP-to-GP ratios to yield very sensitive detection of diseases that affect pulmonary xenon gas exchange. In this work, the spectroscopy and imaging studies were performed at different lung inflation levels. Once ventilation volume validation has been implemented, it will be of great interest to investigate whether the sensitivity of these techniques for detecting lung disease is dependent on lung

inflation and, if so, to determine the inflation level corresponding to maximum sensitivity. Future studies would then all be performed at the same relative inflation level.

Somewhat surprisingly, and unlike the DP-to-GP ratios, the dependence of the estimated septal wall thickness on lung inflation level as characterized by CSSR spectroscopy was, within the accuracy of our measurements, almost negligible. This divergence warrants some additional scrutiny in future studies, but it might already be possible to draw some conclusions. The most obvious is that alveoli do not expand in a balloon-like fashion, stretching the alveolar walls thinner and thinner as they increase in size. Rather, the findings might best agree with a model of alveolar recruitment in which previously closed alveolar ducts open up as the lung expands during inspiration and initially unventilated alveolar sacs fill with gas. Although the septal walls may have been thicker in the closed off state, this would not have contributed to the signals measured by the CSSR acquisition because no HXe would have entered these sacs. This explanation should also serve as a reminder that HXe MRI dissolved-phase measurements are always inherently weighted by the distribution of the HXe magnetization within every volume element. In the case of our spectroscopy studies, this volume encompasses the entire lung. Hence, it is conceivable that some regions, such as the dependent parts of the lung that are relatively poorly ventilated at RV, contribute very little to a globally-averaged parameter value. As a consequence, the MR measurements may deviate from histological findings or from other, differently-weighted, imaging modalities -- a circumstance that can make validation difficult.

In most healthy subjects, the alveolar walls were about 6-8 μm thick. Subjects with COPD or heavy exposure to cigarette smoke tended to have an elevated septal wall thickness relative to the healthy subjects, possibly due to the presence of inflammatory processes. The alveolar wall thickness as quantified by CSSR spectroscopy is a parameter that is independent of the lung tissue density as assessed by CT or hyperpolarized-gas diffusion measurements. In particular, our measurements seem to confirm the biopsy-based findings of inflammatory wall thickening in the presence of emphysematous lesions (40). The insensitivity of the measured septal wall thickness to lung inflation makes the substantial increases found in a subject with a history of high exposure to cigarette smoke all the more remarkable, and suggests that the septal wall thickness may be an interesting biomarker for inflammatory processes at the alveolar level.

Another intriguing finding of the CSSR spectroscopy studies was the changes in the RBC-to-TP ratios in subjects with asthma or COPD relative to healthy subjects. With one exception, all healthy subjects exhibited an RBC-to-TP ratio between 0.24 and 0.32, while the ratios for all subjects with lung disease fell outside this range. In particular, all COPD patients and 4 asthmatics had RBC-to-TP ratios below the range for healthy subjects, but 6 asthmatics were above it. Although the number of subjects is still fairly small, these findings hint at the possibility that the RBC-to-TP ratio could be used for the identification of two distinct groups of asthmatics. The physiologic origins for the measured differences in the RBC-to-TP ratios are currently still unclear. Nevertheless, there are some indications that, at least in the case of the low RBC-to-TP ratios in COPD, these changes appear to be due to a combination of a low RBC volume coupled with an elevated septal wall thickness, as discussed above.

CSSR spectroscopy and 3D DP imaging are conceptually similar techniques but differ in detail. The crucial distinction is that in any given TR within the CSSR pulse sequence, the DP magnetization is initially saturated by RF pulses. As a result, at least ideally, all spectroscopic acquisitions during a breath hold are completely independent from each other and the true HXe accumulation in the lung parenchyma and the blood stream is assessed directly. In a 3D DP acquisition, on the other hand, the flip angle of all RF pulses are much lower than 90° because DP excitation flip angles approaching 90° would quickly depolarize the GP magnetization through exchange and, therefore, cannot be used in an acquisition scheme that requires a large number of RF excitations. Hence, the images reflect the steady-state of an imprecisely known spatial distribution of the xenon magnetization, which depends on physiological parameters such as the septal wall thickness and pulmonary blood flow, and also the flip angle and TR (28). Our simulations indicate that, at least for the MR pulse-sequence parameters selected for our studies, the 3D DP imaging results are strongly coupled to the CSSR measurements by the septal wall thickness, which is not known a priori. However, the price to be paid for the more easily interpreted CSSR spectroscopy measurements is the lack of regional information. In addition, when spectroscopic and imaging results are to be compared, care should be taken to flush HXe from the major airways to prevent systematic errors, since the signal from the airways can be excluded from image analysis but not from global spectroscopic measurements.

Despite the differences between the techniques, the whole-lung RBC-to-TP ratios obtained from the CSSR acquisitions at a 100-ms delay time and from the 3D DP acquisitions were generally consistent. (The other DP ratios are not comparable between the two techniques do due fundamental differences in the excitation of the GP resonance.) The variations within the healthy group were relatively small, and the RBC-to-TP values measured by both techniques in the same subjects were relatively close, with a mean difference of 0.037 as shown in Fig. 9. Values measured by 3D DP acquisitions were generally larger, which is reasonable because the 3D DP acquisitions were performed at a lower lung inflation level. For both techniques, COPD GS 2 and 3 subjects (e.g. COPD subjects C3 and C4) showed much lower RBC-to-TP ratios than healthy subjects, which could be associated with vascular pruning (41) or thickening of septal walls (14). Finally, asthmatics could be classified into 2 subcategories that either had higher (e.g. asthma subject A3) or lower (e.g. asthma subject A4) RBC-to-TP ratios than healthy subjects. The distinction between these two groups is unclear but we speculate that the elevated RBC-to-TP ratio might be related to cardiovascular compensation for decreased gas uptake or to angiogenesis (42), while the decreased RBC-to-TP ratios could be caused by similar factors as in the COPD subjects (43). The good qualitative agreement between the two techniques was not entirely surprising, because the RBC-to-TP ratio is fairly independent of τ, especially when compared to the TP-to-GP and RBC-to-GP ratios, which, for $\tau < 100$ ms, increase rapidly with τ.

Based on the 3D DP acquisitions, the whole-lung DP-to-GP ratios obtained in subjects with obstructive lung disease were lower than those in healthy subjects (mean 0.97% vs. 1.38%, $p < 0.005$; Fig. 5), which indicates a decreased overall xenon gas uptake. Interestingly, all young asthmatics and subjects with COPD at GS 1 had RBC-to-GP ratios within or close to the range of healthy subjects in the imaging studies, possibly due to the early stage of the

disease or to compensatory mechanisms. On the other hand, the RBC-to-GP ratios for the older asthmatic and the COPD subjects at GS 2 and 3 were much lower than those in healthy subjects, suggesting impaired gas exchange in the lungs. These observations were highly consistent with the DLCO/Va results as shown in Fig. 7, although DLCO/Va results were only available in some of the subjects. The TP-to-GP ratio decrease found in almost all subjects with lung disease might be attributed to decreased surface-to-volume ratios due to emphysematous tissue destruction and/or lung hyperexpansion. The signal distribution in the TP-to-GP ratio maps was inhomogeneous for most COPD subjects (except COPD subject C2), but homogenously low for asthmatics with the exception of the older asthmatic subject A4. Thus, although asthma is frequently apparent as regional ventilation defects in ventilation scans, it may also have a global component that affects the entire lung.

A future development may be the combination of CSSR spectroscopy and 3D DP imaging, for example, by borrowing ideas from the Multiple-exchange-time Xenon polarization Transfer Contrast (MXTC) MRI technique (44), which collects exchange contrasts from 3 or 4 delay times and then fits the data to a theoretical gas exchange model to extract physiological lung parameters. A similar approach of obtaining 3D DP images for several different parameter combinations, possibly spread out across multiple breath holds, may allow the quantification of the alveolar wall thickness, tissue density, blood flow, etc. Conversely, spatial localization could be added to CSSR spectroscopy, for instance, by using multi-channel receiver coils, with each coil collecting a separate regional spectrum (45).

In conclusion, CSSR spectroscopy and 3D DP image acquisitions using HXe show a high potential for evaluating lung function and for phenotypic differentiation of lung diseases. The results from both techniques were generally consistent among healthy subjects, COPD subjects and asthmatics. Simulation results indicate that for the MR pulse-sequences used, 3D DP imaging depicts xenon gas-uptake properties by the lung equivalent to short delay-time (tens of milliseconds to about 100 ms) CSSR spectroscopy, depending on the thickness of the septal walls. While CSSR spectroscopy offers better-defined parameter quantification, 3D DP imaging provides regional assessment of lung pathologies.

Acknowledgments

Grant Support: Supported by NIH grant R01 HL109618 from the National Heart, Lung, and Blood Institute, and by Siemens Medical Solutions. The content is solely the responsibility of the authors and does not necessarily represent the official views of the National Heart, Lung, and Blood Institute or the National Institutes of Health.

ABBREVIATIONS USED

COPD	chronic obstructive pulmonary disease
CSSR	chemical shift saturation recovery
RBC	red blood cell
GS	GOLD Stage, global initiative for chronic obstructive lung disease
XTC	xenon polarization transfer contrast
MXTC	multiple-exchange-time xenon polarization transfer contrast

RV	residual volume
FVC	forced vital capacity
TLC	total lung capacity
FEV_1	forced expiratory volume in one second
FID	free induction decay.

REFERENCES

1. Salerno M, Altes TA, Mugler JP 3rd, Nakatsu M, Hatabu H, de Lange EE. Hyperpolarized noble gas MR imaging of the lung: potential clinical applications. Eur J Radiol. 2001; 40(1):33–44. [PubMed: 11673006]
2. van Beek EJ, Wild JM, Kauczor HU, Schreiber W, Mugler JP 3rd, de Lange EE. Functional MRI of the lung using hyperpolarized 3-helium gas. J Magn Reson Imaging. 2004; 20(4):540–554. [PubMed: 15390146]
3. Fain S, Schiebler ML, McCormack DG, Parraga G. Imaging of lung function using hyperpolarized helium-3 magnetic resonance imaging: Review of current and emerging translational methods and applications. J Magn Reson Imaging. 2010; 32(6):1398–1408. [PubMed: 21105144]
4. Mugler JP 3rd, Altes TA. Hyperpolarized 129Xe MRI of the human lung. Journal of magnetic resonance imaging: JMRI. 2013; 37(2):313–331. [PubMed: 23355432]
5. Hersman FW, Ruset IC, Ketel S, Muradian I, Covrig SD, Distelbrink J, Porter W, Watt D, Ketel J, Brackett J, Hope A, Patz S. Large production system for hyperpolarized 129Xe for human lung imaging studies. Acad Radiol. 2008; 15(6):683–692. [PubMed: 18486005]
6. Abraham MH, Kamlet MJ, Taft RW, Doherty RM, Weathersby PK. Solubility properties in polymers and biological media. 2. The correlation and prediction of the solubilities of nonelectrolytes in biological tissues and fluids. Journal of medicinal chemistry. 1985; 28(7):865–870. [PubMed: 4009609]
7. Miller KW, Reo NV, Schoot Uiterkamp AJ, Stengle DP, Stengle TR, Williamson KL. Xenon NMR: chemical shifts of a general anesthetic in common solvents, proteins, and membranes. Proc Natl Acad Sci U S A. 1981; 78(8):4946–4949. [PubMed: 6946442]
8. Mugler JP 3rd, Driehuys B, Brookeman JR, Cates GD, Berr SS, Bryant RG, Daniel TM, de Lange EE, Downs JH 3rd, Erickson CJ, Happer W, Hinton DP, Kassel NF, Maier T, Phillips CD, Saam BT, Sauer KL, Wagshul ME. MR imaging and spectroscopy using hyperpolarized 129Xe gas: preliminary human results. Magn Reson Med. 1997; 37(6):809–815. [PubMed: 9178229]
9. Sakai K, Bilek AM, Oteiza E, Walsworth RL, Balamore D, Jolesz FA, Albert MS. Temporal dynamics of hyperpolarized 129Xe resonances in living rats. J Magn Reson B. 1996; 111(3):300–304. [PubMed: 8661297]
10. Ruppert K, Brookeman JR, Hagspiel KD, Driehuys B, Mugler JP 3rd. NMR of hyperpolarized (129)Xe in the canine chest: spectral dynamics during a breath-hold. NMR Biomed. 2000; 13(4): 220–228. [PubMed: 10867700]
11. Wagshul ME, Button TM, Li HF, Liang Z, Springer CS, Zhong K, Wishnia A. In vivo MR imaging and spectroscopy using hyperpolarized 129Xe. Magn Reson Med. 1996; 36(2):183–191. [PubMed: 8843370]
12. Butler JP, Mair RW, Hoffmann D, Hrovat MI, Rogers RA, Topulos GP, Walsworth RL, Patz S. Measuring surface-area-to-volume ratios in soft porous materials using laser-polarized xenon interphase exchange nuclear magnetic resonance. J Phys Condens Matter. 2002; 14(13):L297–304. [PubMed: 12741395]
13. Driehuys B, Cofer GP, Pollaro J, Mackel JB, Hedlund LW, Johnson GA. Imaging alveolar-capillary gas transfer using hyperpolarized 129Xe MRI. Proc Natl Acad Sci U S A. 2006; 103(48): 18278–18283. [PubMed: 17101964]

14. Dregely I, Mugler JP 3rd, Ruset IC, Altes TA, Mata JF, Miller GW, Ketel J, Ketel S, Distelbrink J, Hersman FW, Ruppert K. Hyperpolarized Xenon-129 gas-exchange imaging of lung microstructure: first case studies in subjects with obstructive lung disease. J Magn Reson Imaging. 2011; 33(5):1052–1062. [PubMed: 21509861]
15. Mansson S, Wolber J, Driehuys B, Wollmer P, Golman K. Characterization of diffusing capacity and perfusion of the rat lung in a lipopolysaccaride disease model using hyperpolarized 129Xe. Magn Reson Med. 2003; 50(6):1170–1179. [PubMed: 14648564]
16. Cleveland ZI, Moller HE, Hedlund LW, Nouls JC, Freeman MS, Qi Y, Driehuys B. In vivo MR imaging of pulmonary perfusion and gas exchange in rats via continuous extracorporeal infusion of hyperpolarized 129Xe. PLoS One. 2012; 7(2):e31306. [PubMed: 22363613]
17. Abdeen N, Cross A, Cron G, White S, Rand T, Miller D, Santyr G. Measurement of xenon diffusing capacity in the rat lung by hyperpolarized 129Xe MRI and dynamic spectroscopy in a single breath-hold. Magnetic resonance in medicine: official journal of the Society of Magnetic Resonance in Medicine / Society of Magnetic Resonance in Medicine. 2006; 56(2):255–264.
18. Patz S, Muradian I, Hrovat MI, Ruset IC, Topulos G, Covrig SD, Frederick E, Hatabu H, Hersman FW, Butler JP. Human pulmonary imaging and spectroscopy with hyperpolarized 129Xe at 0.2T. Acad Radiol. 2008; 15(6):713–727. [PubMed: 18486008]
19. Ruppert K, Mata JF, Brookeman JR, Hagspiel KD, Mugler JP 3rd. Exploring lung function with hyperpolarized (129)Xe nuclear magnetic resonance. Magn Reson Med. 2004; 51(4):676–687. [PubMed: 15065239]
20. Patz S, Muradyan I, Hrovat MI, Dabaghyan M, Washko GR, Hatabu H, Butler JP. Diffusion of hyperpolarized129Xe in the lung: a simplified model of129Xe septal uptake and experimental results. New Journal of Physics. 2011; 13(1):015009.
21. Chang, YV. Toward A Quantitative Understanding of Gas Exchange in the Lung. arXiv: 10083961v1 2010
22. Chang YV. MOXE: a model of gas exchange for hyperpolarized 129Xe magnetic resonance of the lung. Magn Reson Med. 2013; 69(3):884–890. [PubMed: 22565296]
23. Cleveland ZI, Cofer GP, Metz G, Beaver D, Nouls J, Kaushik SS, Kraft M, Wolber J, Kelly KT, McAdams HP, Driehuys B. Hyperpolarized Xe MR imaging of alveolar gas uptake in humans. PloS one. 2010; 5(8):e12192. [PubMed: 20808950]
24. Mugler JP 3rd, Altes TA, Ruset IC, Dregely IM, Mata JF, Miller GW, Ketel S, Ketel J, Hersman FW, Ruppert K. Simultaneous magnetic resonance imaging of ventilation distribution and gas uptake in the human lung using hyperpolarized xenon-129. Proceedings of the National Academy of Sciences of the United States of America. 2010; 107(50):21707–21712. [PubMed: 21098267]
25. Kaushik SS, Freeman MS, Cleveland ZI, Davies J, Stiles J, Virgincar RS, Robertson SH, He M, Kelly KT, Foster WM, McAdams HP, Driehuys B. Probing the regional distribution of pulmonary gas exchange through single-breath gas- and dissolved-phase 129Xe MR imaging. J Appl Physiol. 2013; 115(6):850–860. [PubMed: 23845983]
26. Iguchi S, Imai H, Hori Y, Nakajima J, Kimura A, Fujiwara H. Direct imaging of hyperpolarized 129Xe alveolar gas uptake in a mouse model of emphysema. Magnetic resonance in medicine: official journal of the Society of Magnetic Resonance in Medicine / Society of Magnetic Resonance in Medicine. 2013; 70(1):207–215.
27. Chang YV, Quirk JD, Ruset IC, Atkinson JJ, Hersman FW, Woods JC. Quantification of human lung structure and physiology using hyperpolarized Xe. Magn Reson Med. 2013
28. Ruppert, K.; Mata, JF.; Dregely, I.; Altes, TA.; Miller, GW.; Ketel, S.; Ketel, J.; Ruset, IC.; Hersman, FW.; Mugler, JP, 3rd.. Hyperpolarized xenon-129 dissolved-phase signal dependence on the echo time (abstract). Stockholm: 2010. p. 2552
29. Qing K, Ruppert K, Jiang Y, Mata JF, Miller GW, Shim YM, Wang C, Ruset IC, Hersman FW, Altes TA, Mugler JP 3rd. Regional mapping of gas uptake by blood and tissue in the human lung using hyperpolarized xenon-129 MRI. J Magn Reson Imaging. 2014; 39(2):346–359. [PubMed: 23681559]
30. Tsao J, Jiang Y. Hierarchical IDEAL: fast, robust, and multiresolution separation of multiple chemical species from multiple echo times. Magnetic resonance in medicine: official journal of the

Society of Magnetic Resonance in Medicine / Society of Magnetic Resonance in Medicine. 2013; 70(1):155–159.

31. Shukla Y, Wheatley A, Kirby M, Svenningsen S, Farag A, Santyr GE, Paterson NA, McCormack DG, Parraga G. Hyperpolarized 129Xe magnetic resonance imaging: tolerability in healthy volunteers and subjects with pulmonary disease. Acad Radiol. 2012; 19(8):941–951. [PubMed: 22591724]
32. Driehuys B, Martinez-Jimenez S, Cleveland ZI, Metz GM, Beaver DM, Nouls JC, Kaushik SS, Firszt R, Willis C, Kelly KT, Wolber J, Kraft M, McAdams HP. Chronic obstructive pulmonary disease: safety and tolerability of hyperpolarized 129Xe MR imaging in healthy volunteers and patients. Radiology. 2012; 262(1):279–289. [PubMed: 22056683]
33. Driehuys B, Cates GD, Miron E, Sauer K, Walter DK, Happer W. High-volume production of laser-polarized 129Xe. Applied Physics Letters. 1996; 69(12):1668.
34. Ruppert, K.; Altes, TA.; Mata, JF.; Ruset, IC.; Hersman, FW.; Mugler, JP, 3rd.. Detecting pulmonary capillary blood pulsations using hyperpolarized 129Xe CSSR (abstract). Salt Lake City: 2013. p. 817
35. Matson GB. An integrated program for amplitude-modulated RF pulse generation and re-mapping with shaped gradients. Magnetic resonance imaging. 1994; 12(8):1205–1225. [PubMed: 7854027]
36. Mugler, JP., 3rd; Altes, TA.; Ruset, IC.; Miller, GW.; Mata, JF.; Qing, K.; Tsentalovich, I.; Hersman, FW.; Ruppert, K. Image-based measurement of T2* for dissolved-phase Xe129 in the human lung (abstract). Melbourne: 2012. p. 1347
37. Chan RW, Ramsay EA, Cheung EY, Plewes DB. The influence of radial undersampling schemes on compressed sensing reconstruction in breast MRI. Magnetic resonance in medicine: official journal of the Society of Magnetic Resonance in Medicine / Society of Magnetic Resonance in Medicine. 2012; 67(2):363–377.
38. Sutton BP, Noll DC, Fessler JA. Fast, iterative image reconstruction for MRI in the presence of field inhomogeneities. IEEE transactions on medical imaging. 2003; 22(2):178–188. [PubMed: 12715994]
39. Ruppert, K.; Altes, TA.; Mata, JF.; Ruset, IC.; Hersman, FW.; Mugler, JP, 3rd.. Measuring septal wall thickness in human lung disease using Xe129 CSSR spectroscopy (abstract). Salt Lake City: 2013. p. 1455
40. Vlahovic G, Russell ML, Mercer RR, Crapo JD. Cellular and connective tissue changes in alveolar septal walls in emphysema. American journal of respiratory and critical care medicine. 1999; 160(6):2086–2092. [PubMed: 10588633]
41. Estepar RS, Kinney GL, Black-Shinn JL, Bowler RP, Kindlmann GL, Ross JC, Kikinis R, Han MK, Come CE, Diaz AA, Cho MH, Hersh CP, Schroeder JD, Reilly JJ, Lynch DA, Crapo JD, Wells JM, Dransfield MT, Hokanson JE, Washko GR, Study CO. Computed tomographic measures of pulmonary vascular morphology in smokers and their clinical implications. American journal of respiratory and critical care medicine. 2013; 188(2):231–239. [PubMed: 23656466]
42. Meyer N, Akdis CA. Vascular endothelial growth factor as a key inducer of angiogenesis in the asthmatic airways. Current allergy and asthma reports. 2013; 13(1):1–9. [PubMed: 23076420]
43. Gibson PG, Simpson JL. The overlap syndrome of asthma and COPD: what are its features and how important is it? Thorax. 2009; 64(8):728–735. [PubMed: 19638566]
44. Dregely I, Ruset IC, Mata JF, Ketel J, Ketel S, Distelbrink J, Altes TA, Mugler JP 3rd, Wilson Miller G, William Hersman F, Ruppert K. Multiple-exchange-time xenon polarization transfer contrast (MXTC) MRI: initial results in animals and healthy volunteers. Magn Reson Med. 2012; 67(4):943–953. [PubMed: 22213334]
45. An L, Warach S, Shen J. Spectral localization by imaging using multielement receiver coils. Magn Reson Med. 2011; 66(1):1–10. [PubMed: 21287595]

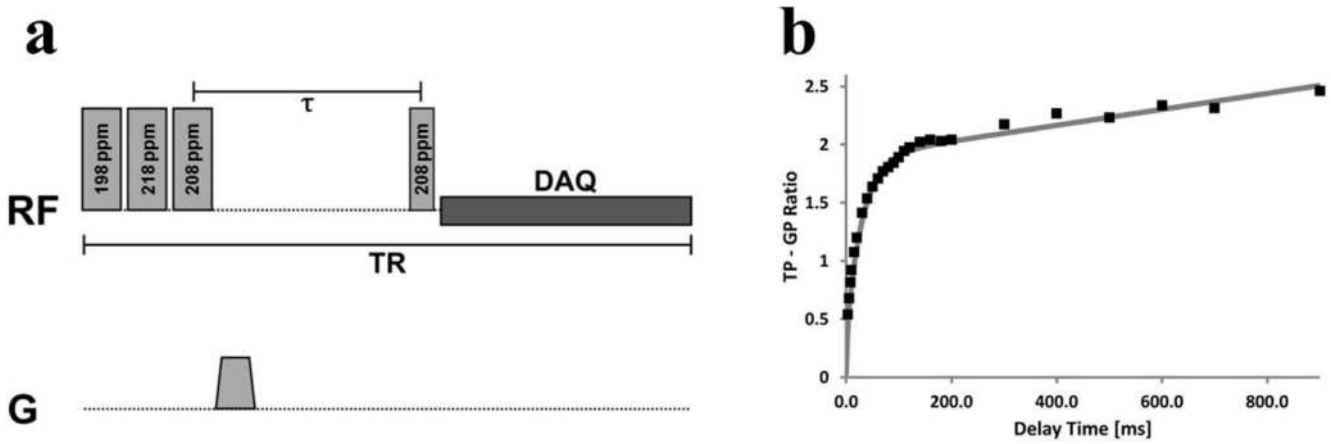

Figure 1.

(**a**) Pulse-sequence diagram for the CSSR spectroscopy acquisition. The DP magnetization is saturated by three narrow-bandwidth RF pulses centered at 198 ppm, 218 ppm and 208 ppm, which leave the GP magnetization largely undisturbed. Following a variable delay time τ an excitation RF pulse centered at 208 ppm is applied and an FID is collected (DAQ). (**b**) Representative xenon saturation-recovery gas-uptake curve (TP-to-GP ratio) as a function of delay time τ. The measurement data (squares) were fitted using a theoretical gas-uptake model described by Patz et al. in (20) (solid line).

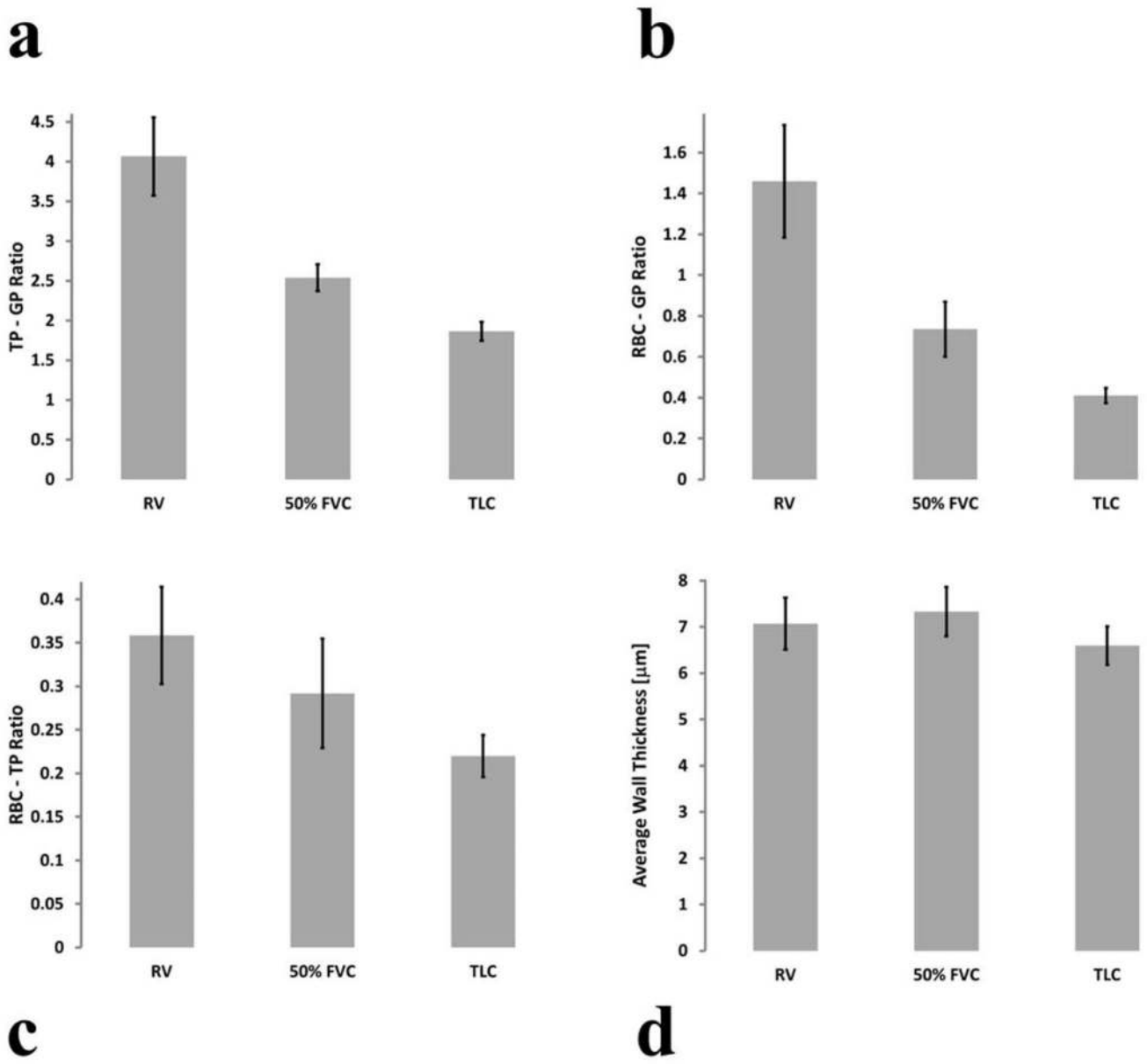

Figure 2.

(**a**) TP-to-GP ratio, (**b**) RBC-to-GP ratio, (**c**) RBC-to-TP ratio and (**d**) average septal wall thickness at 3 lung inflation levels as assessed by CSSR spectroscopy, averaged over 5 healthy subjects. All DP ratios were heavily dependent on lung inflation. At each inflation level, each of the TP-to-GP and RBC-to-GP ratios was significantly different from the others ($p < 0.01$) while the RBC-to-TP ratio was only significantly different between RV and TLC ($p < 0.01$). Changes in the septal wall thickness were not statistically significant.

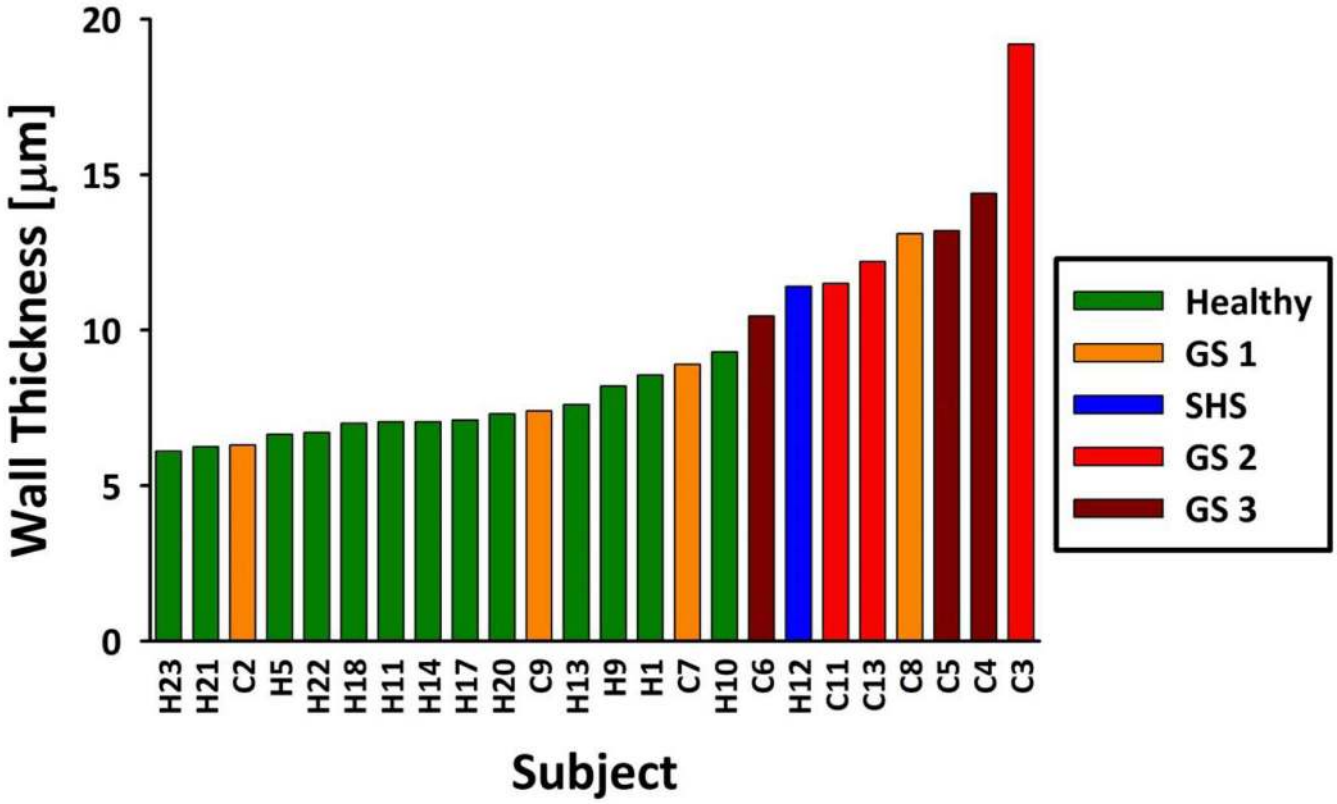

Figure 3.

Healthy subjects (including H12, in blue, who had a high exposure to second-hand smoke) and COPD subjects at various GOLD stages (GS) sorted by average septal wall thickness as measured by CSSR spectroscopy.

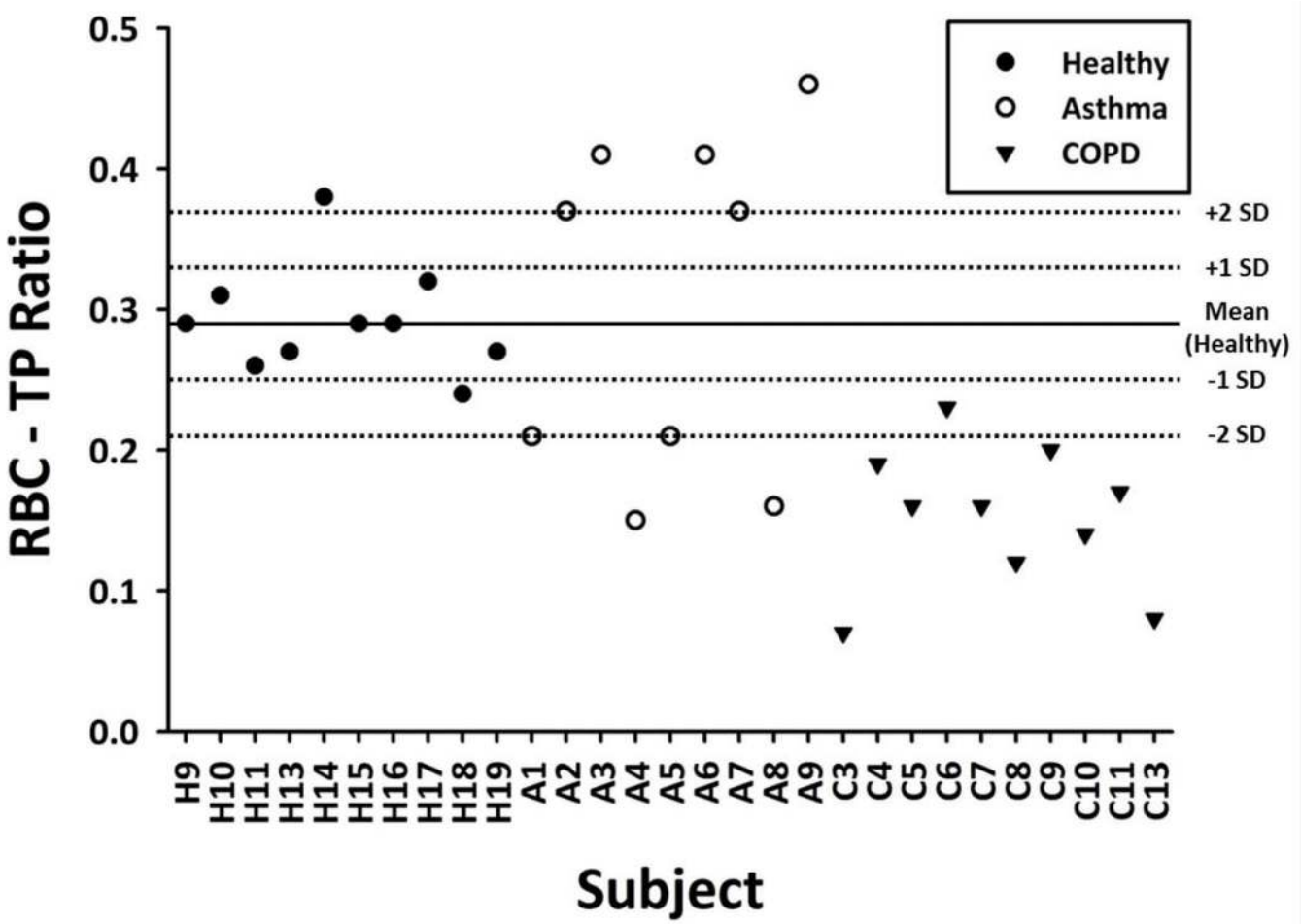

Figure 4.

Average RBC-to-TP ratios obtained from CSSR spectroscopy for healthy (filled circles), asthmatic (open circles) and COPD (triangles) subjects at TLC. The solid line marks the mean value for the healthy subjects while the dashed lines indicate 1 or 2 standard deviations (SD) from the mean. Almost all subjects with lung disease fall outside the 2 standard deviation variation established by the healthy subjects.

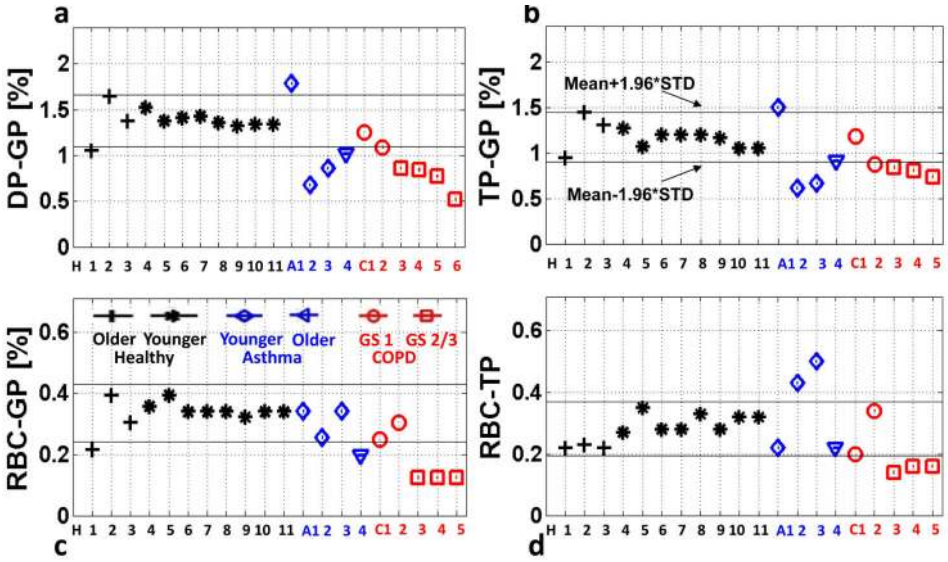

Figure 5.

3D DP Imaging: (**a**) total DP-to-GP, (**b**) TP-to-GP, (**c**) RBC-to-GP, and (**d**) RBC-to-TP ratios, averaged over the whole lung, for all subjects. Healthy subjects and asthma subjects are shown in black and blue, respectively, including the younger and older sub-groups. COPD subjects are shown in red, including GOLD stage 1 (GS 1) represented by round markers, and stages 2 and 3 (GS 2/3) represented by rectangular markers. COPD subject C6 had difficulty inhaling the total volume of gas, which resulted in a relatively low SNR in the third echo of DP images. As a consequence, the TP and RBC components could not be separated for this subject and only the DP-to-GP ratios are included. The 95% confidence intervals based on the results from all healthy subjects are indicated by solid black lines (STD = standard deviation).

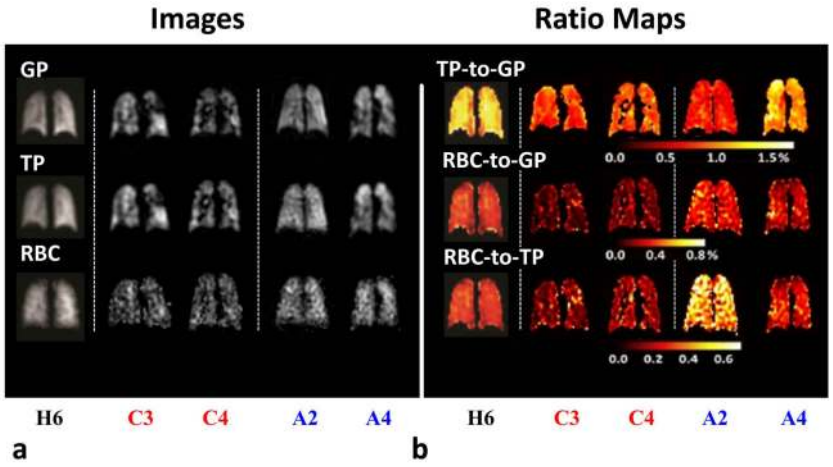

Figure 6.

(**a**) Images of HXe lung ventilation and HXe dissolved in TP and RBC compartments. (**b**) Corresponding TP-to-GP, RBC-to-GP and RBC-to-TP ratio maps acquired in healthy subject H6, COPD subjects C3 and C4, and asthma subjects A2 and A4. COPD subjects C3 and C4 showed numerous ventilation defects and had all ratios lower than those for the healthy subjects. Younger asthma subject A2 showed high RBC-to-TP ratios, as compared with healthy subjects. Similar to COPD subjects C3 and C4, the older asthma subject A4 had all ratios lower than those for the healthy subjects. In the apex of the right lung, this subject had high TP-to-GP ratios and low RBC-to-GP and RBC-to-TP ratios. Images adapted from (29) with permission.

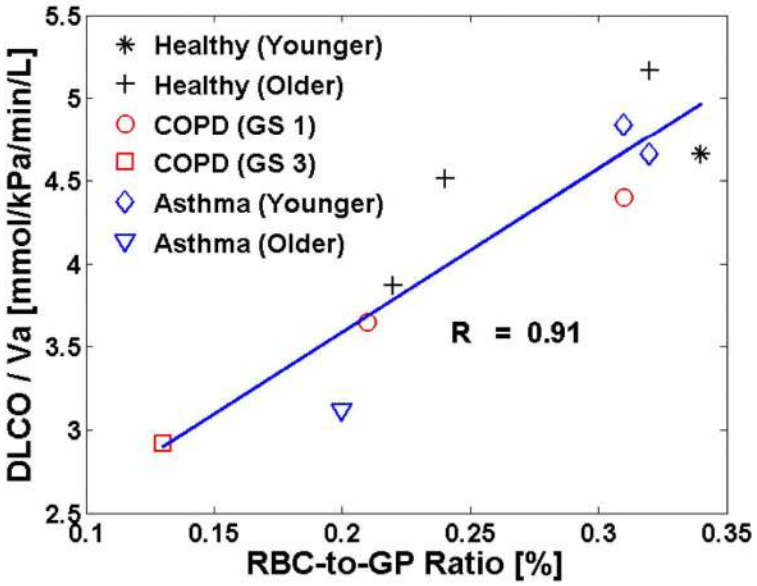

Figure 7.
RBC-to-GP ratios measured by 3D DP imaging versus the DLCO/Va ratios measured by pulmonary function tests.

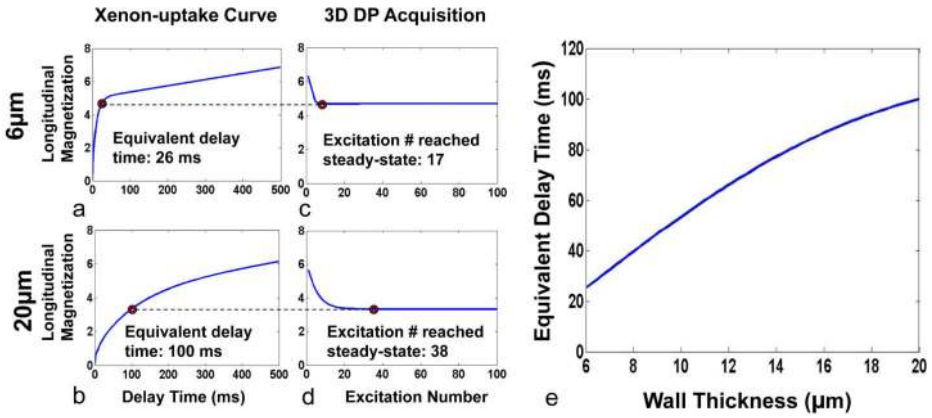

Figure 8.

Simulation results: (**a, b**) Dissolved-phase Xe129 gas-uptake curves for a septal wall thickness of 6 µm (a) or 20 µm (b). (**c**, **d**) Evolution of the dissolved-phase longitudinal-magnetization for the 3D acquisition at a septal wall thickness of 6 µm (c) or 20 µm (d). (**e**) Equivalent delay time corresponding to the steady state for the 3D acquisition versus septal wall thickness.

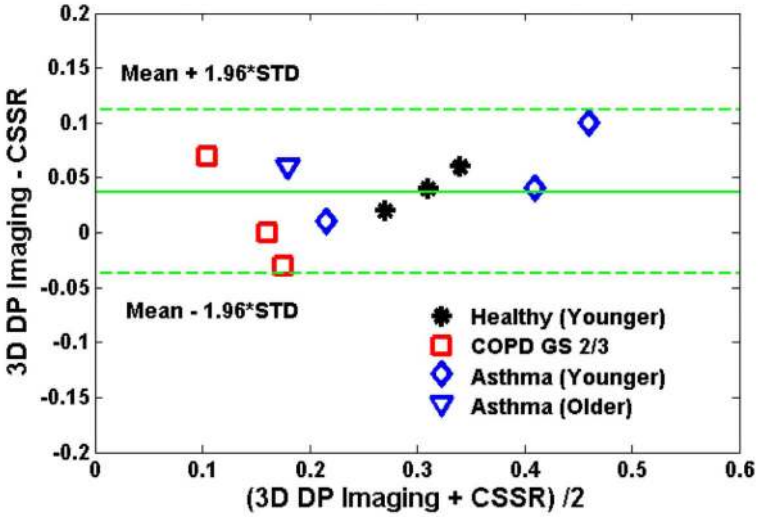

Figure 9.

Bland-Altman plot of the mean RBC-to-TP ratios measured by 3D DP imaging at a lung inflation level of one-third FVC and by CSSR spectroscopy at TLC. The mean of the ratio difference (3D DP Imaging – CSSR spectroscopy) was 0.037 ± 0.036.

Table 1

Subject Demographics and Pulmonary Function Test Results

Subject	Age	Sex	FEVi %pred	FEVi/FVC	DLCO/Va (mmol/kPa/min/L)
H1	54	M	128	0.75	4.66
H2	55	F	124	0.79	5.17
H3	59	F	101	0.80	4.51
H4	18	F	119	0.87	
H5	21	F	105	0.86	
H6	21	F	105	0.86	
H7	21	F	91	0.81	4.66
H8	21	F	96	0.75	
H9*	32	F	95	0.80	
H10*	25	F	94	0.86	
H11*	21	F	92	0.75	
H12	50	F	110	0.75	
H13	21	F	107	0.91	
H14	21	M	98	0.79	
H15	26	F	117	0.83	
H16	26	F	102	0.84	
H17	21	F	86	0.86	
H18	23	F	102	0.80	
H19	25	M	107	0.83	
H20	21	F	92	0.83	
H21	26	F	117	0.83	
H22	33	F	86	0.76	
H23	20	F	103	0.90	
C1	55	F	96	0.69	3.65
C2	40	F	83	0.69	4.40
C3*	56	F	64	0.54	
C4*	55	F	39	0.57	2.92
C5*	58	F	30	0.50	
C6*	58	M	46	0.42	2.58
C7	24	M	87	0.64	
C8	62	M	52	0.72	
C9	62	M	90	0.71	
C10	59	M	60	0.71	
C11	59	M	66	0.68	
C12	48	M	68	0.73	
C13	40	M	51	0.66	
A1*	22	F	67	0.73	4.84

Subject	Age	Sex	FEVi %pred	FEVi/FVC	DLCO/Va (mmol/kPa/min/L)
A2*	16	M	100	0.73	
A3*	26	M	80	0.60	4.66
A4*	53	M	89	0.57	3.12
A5	45	M	83	0.79	
A6	22	F	71	0.73	
A7	28	F	100	0.67	
A8	57	F	52	0.56	
A9	49	F	48	0.49	

H denotes healthy subjects, C denotes COPD subjects, and A denotes asthma subjects. Subjects marked by * underwent both 3D DP imaging and CSSR spectroscopy. For each category (H, C or A), subjects before the first subject marked by * underwent only 3D DP imaging, and subjects after the last subject marked by * underwent only CSSR spectroscopy.